Research Square

Preprints are preliminary reports that have not undergone peer review.
They should not be considered conclusive, used to inform clinical practice,
or referenced by the media as validated information.

Valence-Free Open Nanoparticle Superlattices

David Vaknin

vaknin@ameslab.gov

Iowa State University https://orcid.org/0000-0002-0899-9248

Binay Nayak

Iowa State University https://orcid.org/0000-0002-3995-4114

Wenjie Wang

Iowa State University

Prapti Kakkar

Iowa State University

Honghu Zhang

Brookhaven National Lab https://orcid.org/0000-0003-1784-7825

Zinnia Mallick

South Dakota School of Mines and Technology https://orcid.org/0009-0000-1318-5401

Shan Zhou

South Dakota School of Mines and Technology https://orcid.org/0000-0002-6476-3280

Dmytro Nykypanchuk

Brookhaven National Laboratory

Surya Mallapragada

Iowa State University https://orcid.org/0000-0002-9482-7273

Alex Travesset

Iowa State University

Article

Keywords:

Posted Date: August 18th, 2025

DOI: https://doi.org/10.21203/rs.3.rs-7256208/v1

License: This work is licensed under a Creative Commons Attribution 4.0 International License.
Read Full License

Additional Declarations: There is **NO** Competing Interest.

Version of Record: A version of this preprint was published at Nature Communications on January 17th, 2026. See the published version at https://doi.org/10.1038/s41467-026-68316-4.

Valence-Free Open Nanoparticle Superlattices

Binay P. Nayak,[†] Wenjie Wang,[‡] Prapti Kakkar,[†] Honghu Zhang,[¶] Zinnia Mallick,[§] Shan Zhou,[§] Dmytro Nykypanchuk,[‖] Surya K. Mallapragada,[†] Alex Travesset,[*,⊥] and David Vaknin[*,⊥]

[†]*Ames National Laboratory, and Department of Chemical and Biological Engineering, Iowa State University, Ames, IA, 50011, US*

[‡]*Division of Materials Sciences and Engineering, Ames National Laboratory, Ames, IA, 50011, US*

[¶]*NSLS-II, Brookhaven National Laboratory, Upton, NY, 11973, USA*

[§]*Department of Nanoscience and Biomedical Engineering, South Dakota School of Mines and Technology, Rapid City, SD, 57701, USA*

[‖]*Center for Functional Nanomaterials, Brookhaven National Laboratory, Upton, NY, 11973, USA*

[⊥]*Ames National Laboratory, and Department of Physics and Astronomy, Iowa State University, Ames, IA, 50011, US*

E-mail: trvsst@ameslab.gov; vaknin@ameslab.gov

Abstract

A cornerstone of next-generation materials design is establishing a framework for assembling nanoparticle superstructures with tailored symmetries. A longstanding challenge has been assembling diamond-like superstructures for photonic devices. Traditionally, such open superstructures require functionalized nanoparticles with directional or anisotropic interactions, reminiscent of valence bonding in a diamond. Here, we present a robust strategy for assembling valence-free nanoparticles into a broad array of cubic superstructures. By grafting nanoparticles with oppositely charged, end-functionalized water-soluble polymers of adjustable molecular weight, we gain control over electrostatic interactions and conformational constraints. This unified approach yields lattices analogous to rock salt, CsCl, zinc-blende, diamond, and the exceptionally rare simple cubic phase, with tunable lattice constants. Theoretical models and simulations elucidate the underlying interactions, unlocking novel avenues for engineering valence-free nanoparticle superlattices.

Introduction

Assembling colloidal nanoparticles (NPs) into cubic superstructures has long been a central challenge in nanoscience.[1–9] For example, the fabrication of diamond-like superstructures has traditionally relied on patchy or anisotropic NPs, with directional interaction sites.[10,11] The "valence"-like bonding mimics the directional bonding observed in carbon-based diamond structures. Various methods have been employed to achieve this goal, including the arrangement of NPs within tetrahedral DNA origami cages[10] and the assembly of micron-sized tetrahedral clusters linked through DNA.[11] DNA origami tetrapods have also been used to create diamond lattices with photonic band gaps.[12] Only report of a diamond superlattice, assembled without valence, exhibited broad X-ray diffraction peaks, signaling poor structural quality.[13] Given these challenges, we present a general strategy for assembling a diverse array of NP superlattices, in-

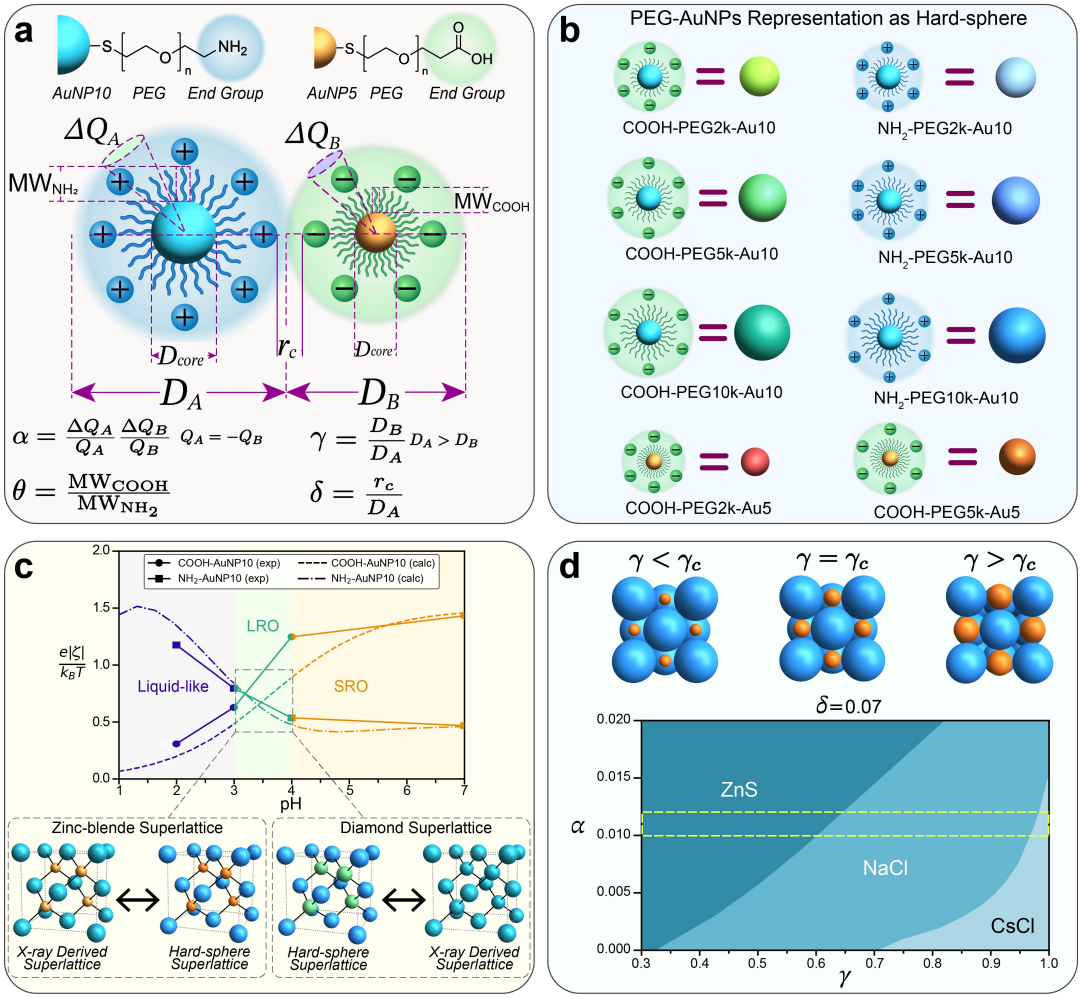

Fig. 1. Strategy to construct valence-free ionic-like nanoparticle superlattices. (**a**) Depiction of AuNPs with core sizes of 5 nm (yellow) and 10 nm (blue) are functionalized with PEG terminated with either —NH_2 (blue) or —COOH (green). The surface charges on the blue (+) and the green (−) PEG corona are indicated consistently. D_A and D_B denote the actual hard sphere diameters of grafted AuNPs, with their ratio defined as $\gamma = \frac{D_B}{D_A}$. To account for local electrostatic interactions, spherical-angle charges corresponding to charge fractions ΔQ_A and ΔQ_B are considered at a nearest-neighbor distance r_c. The parameter θ represents the molecular weight ratio of the grafted PEG chains. (**b**) Legend for identifying the various nanoparticles used to assemble the reported superlattices. The spheres on the right depict the effective hard sphere diameter after grafting AuNP with 2, 5, and 10 kDa PEG. (**c**) (Top) Normalized ζ-potential as a function of pH for PEG-AuNPs, with PEG terminated by either —NH_2 (squares) or —COOH (circles). Dashed and dash-dotted lines, representing predictions from electrostatic model calculations (detailed in the SI), are also shown. The pH from 3 to 4 region of overlapping lines is optimal for inducing the assembly of high-quality superlattices. (Bottom) Ideal zinc-blende and diamond structures derived from X-ray analysis are presented alongside the corresponding actual grafted-AuNP assemblies depicted in B. In the zinc-blende structure, distinct colors highlight the two different particle types, whereas in the diamond structure, the spheres are shown in a uniform color, reflecting that the X-ray pattern arises predominantly from identical AuNP cores. Henceforth, structures with uniform core sizes (e.g., diamond, simple cubic, and BCC) are depicted with their actual grafted PEG using the symbols from B. (**d**) (Top) (110) plane view of a rock-salt lattice for different γ values, illustrating ideal hard sphere contacts at $\gamma = \gamma_c$. (Bottom) A proposed phase diagram based on geometrical constraints and electrostatic interactions that guide the assembly of various superlattices. The dashed lines indicate the region that aligns with our experimental observations.

cluding diamond, inspired by binary ionic compounds, achieved without relying on valence.

Binary ionic compounds exhibit a rich diversity of ordered structures dictated by ion size.[14,15] For example, similar-size ions such as Cs^+ and Cl^- tend to adopt simple cubic or pseudo-body-centered cubic (BCC)-like arrangements. For moderate size asymmetry, as seen with Na^+/K^+ and Cl^-, the prevailing configuration is a rock salt or face-centered cubic (FCC)-like structure. Divalent compounds with higher size asymmetry, from oxides like CaO and BaO to chalcogenides such as ZnS, follow a similar trend.[16] Notably, ZnS can crystallize in a zinc-blende (FCC) or wurtzite (hexagonal) lattice, depending on external conditions.[17] Hypothetically, if the rock salt, cesium chloride, or zinc-blende structures were made with *iden-*

tical elements, they would correspond to simple cubic, BCC, and diamond lattices, respectively.

Building on these structural insights, we now explore how similar principles apply to the assembly of spherical NPs. We functionalize NPs with poly(ethylene glycol) (PEG) chains terminated with carboxyl ($-$COOH) or amine ($-NH_2$) end-groups, enabling control over their surface charge through adjustment of pH. This strategy is broadly applicable, as both the NP type and the terminal groups can be generalized to any system employing ligands with oppositely charged ends. Moreover, by varying the molecular weight of PEG, we tune the polymer chain length and, consequently, the hydrodynamic size of the grafted NPs. The resulting superlattices consist of NP cores embedded within a uniform polymeric matrix. When the NP cores are identical, the structures can adopt simpler forms such as BCC, simple cubic, or diamond arrangements, which are analogous to elemental binary ionic salts, depending on their hydrodynamic size. The key insight is that the hydrodynamic radius, tuned via polymer chain length, sets the effective ion size, and thus the structure and lattice constants are independent of the NP core diameter. Early experiments with micron-sized charged colloids in organic solvents yielded a range of ionic-like superlattices but did not produce ZnS superlattices, a precursor for assembling diamond superlattices.[18] However, theoretical work has shown that valence-free nanoparticles, interacting via designed spherically symmetric potentials, can assemble into open lattices such as diamond and simple cubic.[19,20]

To further illustrate our assembly strategy, we model the grafted NPs as hard spheres with diameters D_A and D_B (with $D_A > D_B$) and uniformly opposite surface charges (Q_A and Q_B). As shown in Fig. 1a, the key parameter is the size ratio;

$$\gamma = \frac{D_B}{D_A} \leq 1. \tag{1}$$

Experimentally, γ is determined as the ratio of the effective modal hydrodynamic diameters of the two NP populations. This γ parameter has also been examined in the context of size-asymmetric binary charged colloidal suspensions (see SI for details).[21] Most ionic superstructures, including the ones discussed above-CsCl, NaCl, and ZnS, exhibit a critical gamma (γ_c) such that for $\gamma > \gamma_c$ each B nanoparticle is surrounded by A nanoparticles, stabilizing the lattice, while for $\gamma \leq \gamma_c$ similar charged A NPs come into contact, leading to structural instability (see Fig. 1d). Detailed calculations in the Supporting Informations (SI) further reveal that the stability of the ZnS structure is significantly enhanced, achieving the highest asymmetric mixture, by tuning the repulsion between like-charged NPs, thereby facilitating the assembly of open structures such as diamond or simple cubic lattices.

Recent 2D assembly experiments for the same binary systems indicate that crystallization occurs within a narrow pH range, typically between 2 and 5.[22] Furthermore, ζ-potential measurements shown in Fig. 1c reveal a regime where NP charges overlap optimally for assembly, and theoretical work demonstrates maximum attraction when NP satisfies $Q_A = -Q_B$. Notably, even if the charges per particle are initially imbalanced, the proximity of the NPs induces a self-regulation that drives the system towards equal and opposite charges, thereby maximizing the attraction.[23] This approach leads to assembling a wide range of NP superlattices by controlling the effective NP charge and hydrodynamic size.

Results and Discussions

Our approach begins with a binary system engineered to favor ZnS-like or NaCl-like superstructures. We use COOH-PEG5k-Au5 and NH_2-PEG10k-Au10 NPs, which yield a size ratio of $\gamma \simeq 0.6$ optimal for a ZnS or NaCl-like superlattices assembly (see Fig. 1d). In addition, we define a parameter θ as

$$\theta = \frac{\mathrm{MW_{COOH}}}{\mathrm{MW_{NH_2}}},$$

representing the ratio of molecular weights (MWs) of the grafted PEGs with different end groups. This parameter is valuable for constructing the experimental phase diagram of the

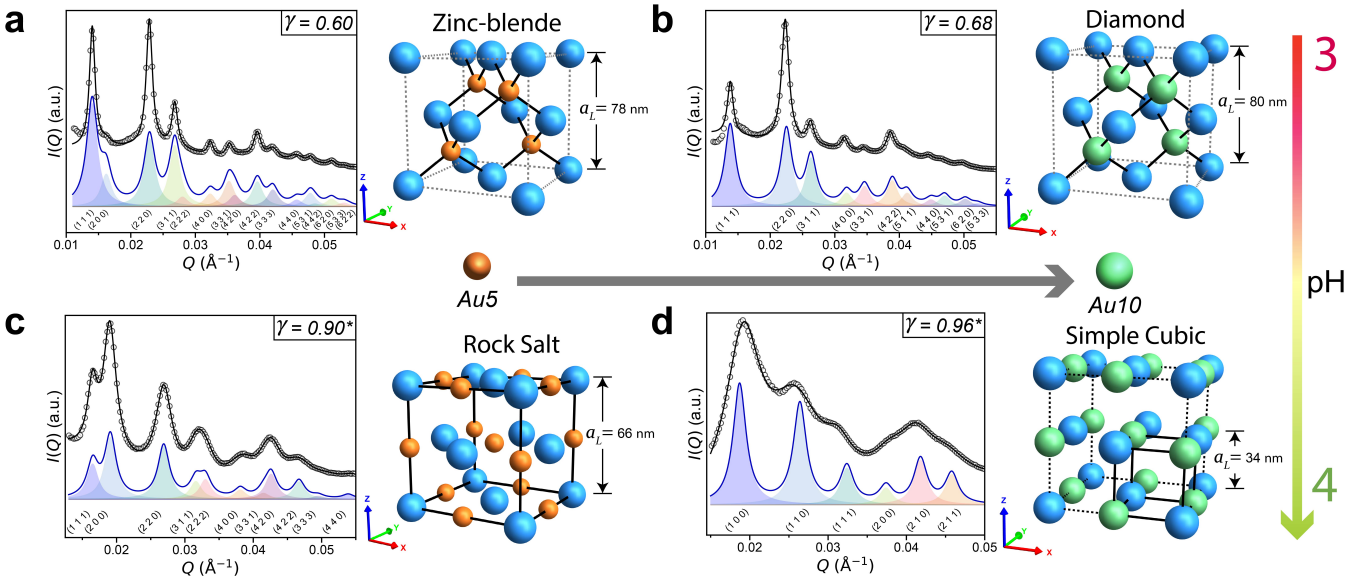

Fig. 2. Transition from Zinc-Blende to Diamond Superstructure. (**a**) SAXS diffraction pattern ($I(Q)$ vs. Q) for COOH-PEG5k-Au5 and NH_2-PEG10k-Au10 at pH 3 (4:1 mixing ratio), fitted using a ZnS-like structural model. The modeled intensity profile (blue solid line) is shown below, with individual contributions highlighted in color. This ZnS-like structure can also be formed from the same binary system with mixing ratios of 1:1, 2:1, and 4:1, as shown in Fig. S6. (**b**) SAXS diffraction pattern for a 2:1 mixture of COOH-PEG5k-Au10 and NH_2-PEG10k-Au10 at pH 3, fitted to a diamond-like structural model. The only change from A to B is that the 5 nm NPs are replaced with 10 nm. This diamond structure can also form with mixing ratios of 1:1 and 4:1 for the same system, as shown in Fig. S8. (**c**) SAXS diffraction pattern for a 2:1 mixture of COOH-PEG5k-Au5 and NH_2-PEG10k-Au10 at pH 4, fitted to a NaCl-like structural model. This NaCl-like structure can also form with mixing ratios of 1:1 and 4:1 for the same system, as shown in Fig. S7. (**d**) SAXS diffraction pattern for a 1:1 mixture of COOH-PEG5k-Au10 and NH_2-PEG10k-Au10 at pH 4, fitted to a simple cubic structural model (blue solid line). This simple cubic structure arises from the identical core sizes (10 nm) of both grafted nanoparticles, differentiating it from the binary NaCl-like structure. Illustrations of the ZnS-like, NaCl-like, diamond-like, and simple cubic superstructures are provided adjacent to their respective diffraction patterns, with the lattice constant (a_L) of each structure indicated in the illustrations. The γ value for each mixture is indicated in the plot. The symbol $*$ represents the γ value estimated from NN distance.

assembled structures described below.

Fig. 2a shows the SAXS diffraction pattern ($I(Q)$ vs. Q) for a 4:1 mixture of COOH-PEG5k-Au5 and NH_2-PEG10k-Au10 at pH 3. The diffraction pattern corresponds to that expected for a ZnS-like (zinc blende) structure, with the modeled intensity profile accurately reproducing the experimental data. Notably, this ZnS-like structure can also form at different mixing ratios (1:1, 2:1, and 4:1), as shown in Fig. S6. Although ZnS-like assemblies consistently exhibit 1:1 stoichiometry, they can arise from mixtures with varying initial ratios of NPs, with any excess particles remaining unincorporated in solution. To achieve a reliable and well-defined diffraction pattern, we initially employed core NPs with distinct sizes (5 nm and 10 nm), thereby leveraging the electron density (ED) contrast between the two NP types to stabilize a ZnS-like lattice. For a binary system consisting of identical 10 nm core NPs ($\gamma = 0.68$), the lack of ED contrast transforms the ZnS-like into a diamond-like superlattice. Our work focuses on the gold NP lattice, treating the polymer scaffold, whose low ED is virtually invisible in X-ray scattering, as negligible. Moreover, the NP dielectric constant, not its polymeric support, dictates the optical properties for photonic applications.[24] This applies to the SAXS diffraction pattern shown in Fig. 2b, which can be accurately fitted to an almost perfect diamond structure. These combinations indicate that optimal ZnS or diamond assembly occurs at $\theta \simeq 0.5$. To further validate the robustness of our self-assembly strategy, we extended our investigation to binary mixtures of 20 and 10 nm AuNPs, functionalized with the same $-$COOH and $-NH_2$ terminated PEG ligands. By maintaining similar γ and θ ratios, these larger particles also assemble into a high-quality zinc-blende superlattice, as confirmed by the SAXS patterns in Fig. S20.

The stability of the zinc-blende structure offers a pathway for assembling diamond lattices. As shown in Fig. 1a, the effective NP hard sphere diameter is defined as the sum of its core

and the PEG corona thickness.[25] By keeping the cores the same and tuning the PEG chain length to achieve γ values within $\gamma_c^{\mathrm{ZnS}} \leq \gamma < \gamma_c^{\mathrm{NaCl}}$, diamond superlattices are formed. In contrast, when γ falls within $\gamma_c^{\mathrm{NaCl}} \leq \gamma < \gamma_c^{\mathrm{CsCl}}$, a simple cubic structure is obtained.

The phase diagram in Fig. 1d depends on the parameter

$$\alpha = \frac{\Delta Q_A}{Q_A}\frac{\Delta Q_B}{Q_B},$$

where ΔQ_A and ΔQ_B denote the fraction of surface charge specified within a specified solid angle where a NP is in contact with a neighboring NP (See Fig. 1a). These localized charge correlations introduce a short-range electrostatic correction to the hard-sphere model, shifting the critical γ values and thereby enhancing the relative stability of ZnS and NaCl lattices over CsCl. The dashed lines in Fig. 1d delineate a confined (α, γ) window corresponding to the optimal conditions for the assembly of the above cubic superstructures. This highlights that tuning the nanoparticle surface charge (and hence α) provides control over the resulting lattice symmetry.

A further essential knob for controlling the superstructure assembly is the effective surface charge of the NPs, which can be finely tuned by adjusting the pH. As shown in Fig. 2c, increasing the pH from 3 to 4 transforms the zinc-blende into a rock-salt superstructure. Similarly, the diamond-like superstructure observed at pH 3 (Fig. 2b) transitions to a simple cubic configuration at pH 4 (Fig. 2d). Notably, this simple cubic phase arises from NPs with identical 10 nm cores, where the loss of ED contrast diminishes the (1 1 1) peak characteristic of a rock-salt lattice. Furthermore, the SAXS pattern of the simple cubic phase exhibits a broad peak, indicative of mesoscale order and structural defects. This imperfect, simple cubic lattice sets the stage for our subsequent pursuit of a defect-free simple cubic structure.

Thus, we explore alternative parameter combinations by maintaining a constant γ while varying θ (MWs of grafted PEG). Some combinations yield simple cubic short-range ordering (SRO). However, setting $\theta \simeq 5$ and $\gamma \simeq 0.8$ (a condition that typically favors a rock-salt structure), the binary mixture of COOH-PEG10k-Au10 and NH_2-PEG2k-Au10 produced a nearly perfect simple cubic analog. Fig. 3a shows the SAXS diffraction pattern of this assembly, which is accurately fitted to a simple cubic model.

By interchanging the terminal groups- swapping COOH and NH_2, we stabilize a high-quality diamond lattice. Fig. 3b presents the SAXS diffraction pattern for a 1:1 mixture of COOH-PEG2k-Au10 and NH_2-PEG10k-Au10 at pH 3 ($\theta \simeq 0.2$), which is well-fitted to a diamond-like structure. This modification alters both the total and local charge on the NPs, as grafting density (and thus surface charge) depends on PEG chain length.[26,27] Moreover, the effective size ratio γ shifts from 0.80 (yielding a simple cubic lattice) to 0.64 (to a diamond lattice), in accordance with the calculated phase diagram in Fig. 1D. These findings emphasize that maintaining low θ and γ values is essential for stabilizing a diamond lattice, whereas higher values typically favor a rock-salt structure. We have successfully assembled a variety of diamond and zinc-blende lattices using these parameter regimes (see SI Figs. S12 and S14).

Our next binary system exhibits the unique phenomenon of particle fractionalization, a process in which NPs are selectively sorted by size from their inherent polydispersity (See SI for detailed discussions).[28,29] Fig. 3c shows the SAXS diffraction pattern for a binary mixture of COOH-PEG10k-Au10 and NH_2-PEG5k-Au10 with $\theta \simeq 2$ and $\gamma \simeq 0.97$, conditions that would typically yield a simple cubic pattern given the use of identical core NPs. However, the appearance of a weak (111) peak, characteristic of a NaCl-like structure (see Fig. 2b), indicates that the assembly process is selective, assigning distinct particle sizes to different lattice sites through fractionalization. This slight size disparity results in a weak (111) reflection analogous to the differences observed between the diffraction patterns of NaCl and KCl, where reduced ED contrast in KCl produces a similar effect despite both crystallizing in an FCC structure.

Based on the phase diagram in Fig. 1d, we identified a narrow range of parameters that

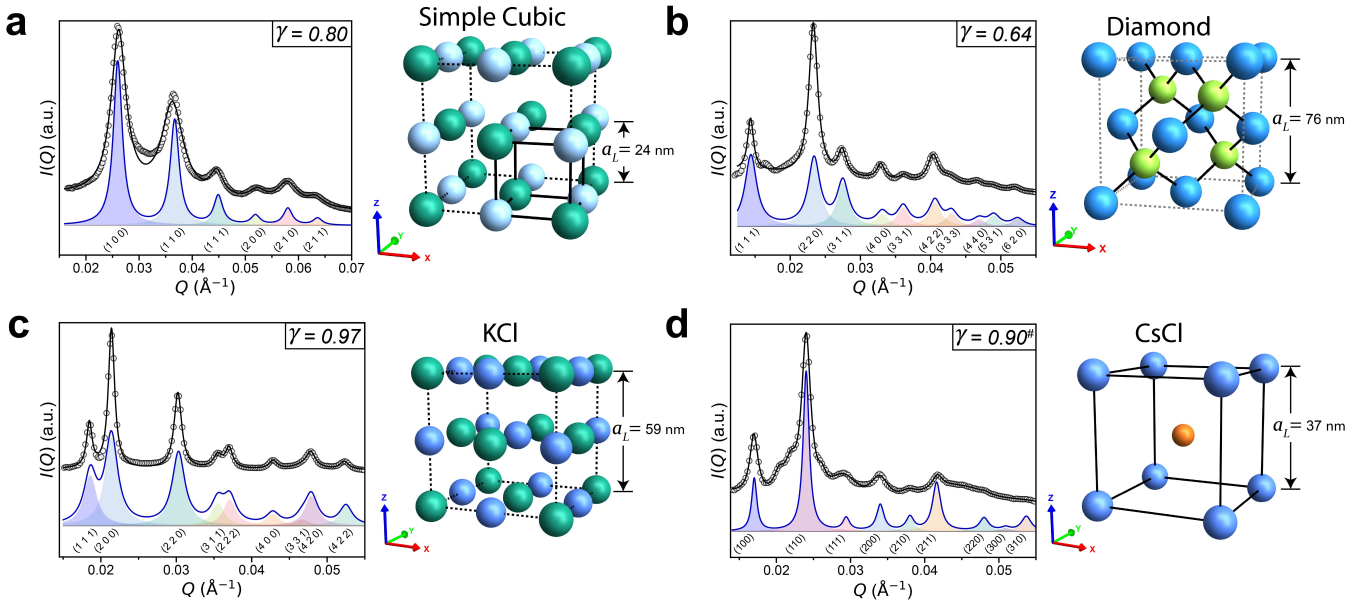

Fig. 3. Simple Cubic and Cesium-chloride like Superstructures. (**a**) SAXS diffraction pattern ($I(Q)$ vs. Q) for a 1:1 mixture of COOH-PEG10k-Au10 and NH_2-PEG2k-Au10 at pH 3, fitted to a simple cubic structural model. The modeled intensity profile (blue solid line) and individual peak contributions are indicated. Notably, this simple cubic structure is effectively equivalent to the NaCl-like arrangement; however, due to the similar core sizes of the nanoparticles, the X-ray scattering detects it as a simple cubic structure. (**b**) SAXS diffraction pattern for a 1:1 mixture of COOH-PEG2k-Au10 and NH_2-PEG10k-Au10 at pH 3, fitted to a diamond-like structural model (blue solid line). This diamond structure is achieved by swapping the grafted PEG terminal groups in A. (**c**) SAXS diffraction patterns for a 1:2 mixture of COOH-PEG10k-Au10 and NH_2-PEG5k-Au10 at pH 3, fitted to a KCl-like structural model. The modeled intensity profile (blue solid line) and color-coded contributions are shown below. While the expected structure is a simple cubic arrangement derived from the NaCl-like structure, nanoparticle fractionalization leads to a preference for the KCl-like structure. (**d**) SAXS diffraction pattern of 1:2 mixture of NH_2-PEG5k-Au10 and COOH-PEG5k-Au5 at pH 3, fitted to a CsCl-like structure. Illustrations of the NaCl-like, diamond-like, CsCl-like, and simple cubic superstructures are provided adjacent to their respective diffraction patterns, with the lattice constant (a_L) indicated in each illustration. The γ value for each mixture is indicated in the plot. The symbol # represents the γ value estimated from D_H as described in SI.

yield a CsCl-like structure. By selecting a binary mixture of COOH-PEG5k-Au10 and NH_2-PEG5k-Au5 NPs ($\gamma \simeq 0.9$ and $\theta \simeq 1$), parameters that lie near the predicted coexistence region for NaCl and CsCl superstructures, and by tuning the pH to 3, we successfully assembled a CsCl-like superlattice. Fig. 3d presents the SAXS diffraction pattern for this mixture at pH 3, which fits well to a CsCl-like structure. Small satellite peaks near the prominent (110) reflection indicate systematic defects, as discussed in detail in the SI. In contrast, using NPs with identical core sizes (10 nm and 10 nm) under the same grafting conditions to achieve a BCC superstructure resulted only in low-quality, short-range BCC-like ordering, as shown in Fig. S17. The phase diagram in Fig. 4b justifies this finding by revealing that the CsCl/BCC phase is stable only within a very narrow parameter window.

To rationalize and extend our experimental findings, we introduce the following semi-quantitative free energy expression, which incorporates electrostatic correlations:

$$E_L = \frac{\mathcal{N}_P}{2} \frac{e^2 Q_A^2}{4\pi\varepsilon_0 D_A} \left(\frac{2M_L}{1+\gamma} + \frac{\alpha\, n_{AA}/2}{\delta + c_L(\gamma - \gamma_c)} \right). \quad (2)$$

Here, γ, γ_c, α, and δ are defined in Fig. 1a; M_L represent the Madelung energy of the corresponding lattice; c_L is a constant, and n_{AA} denotes the number of nearest neighbors for an A nanoparticle. The second term in parentheses accounts for the short-range repulsion between $B-B$ NPs as γ approaches γ_c. Notably, increasing α enhances this $B-B$ repulsion, thereby improving the stability of the ZnS structure by effectively shifting γ_c to a higher value (see Fig. 1d). A detailed discussion of this model is provided in the SI.

Understanding the assembly process requires elucidating the molecular-level mechanisms governing NP interactions, particularly the attraction of $A-B$ NPs and the repulsion of $B-B$ (and $A-A$) NPs described in Eq. 2.

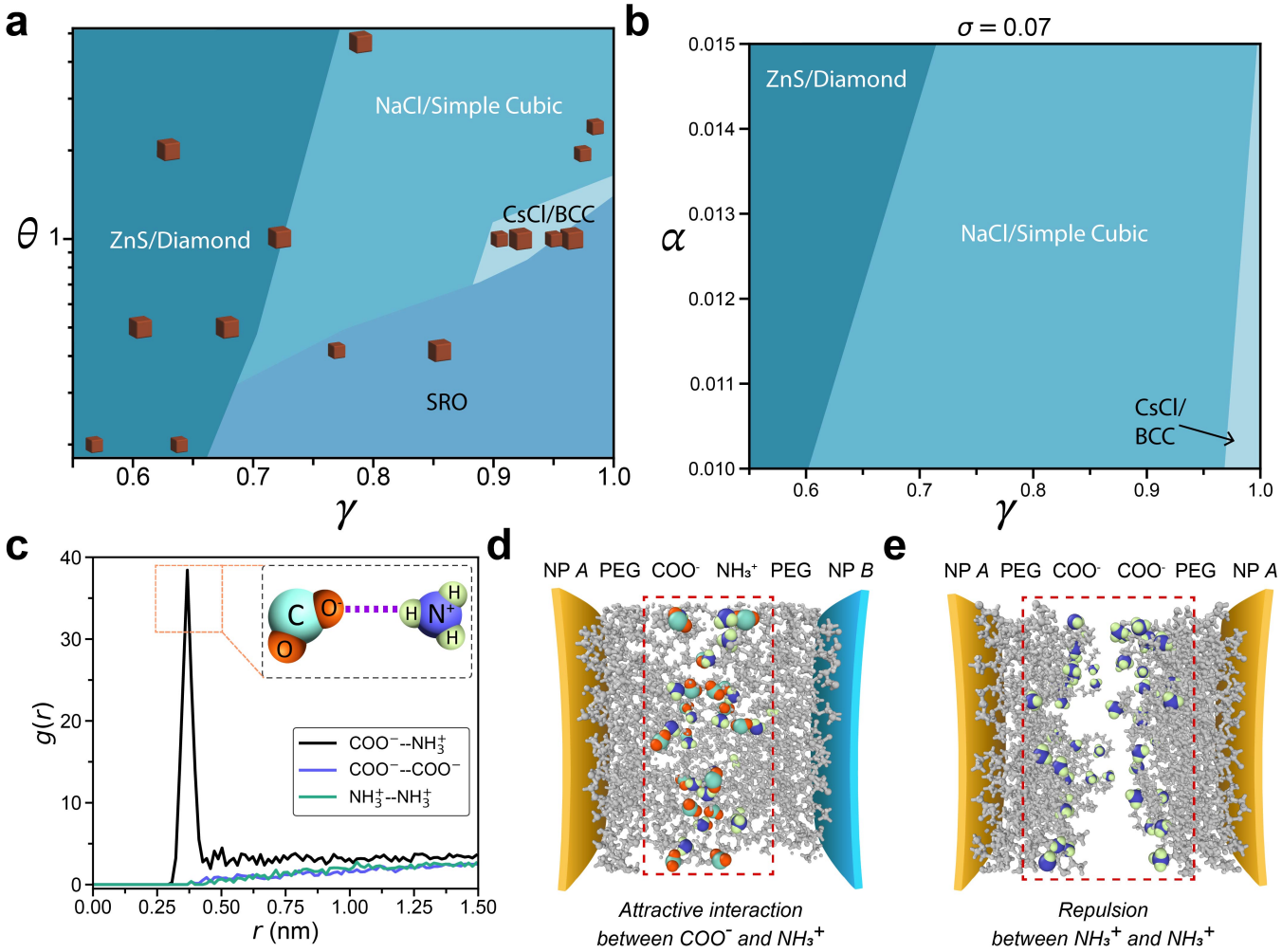

Fig. 4. Experimental, Theoretical Phase Diagrams and Molecular Simulations. (**a**) SAXS-derived experimental phase diagram of cubic superstructures plotted as a function of θ versus γ. Larger cube symbols indicate binary mixtures containing 10 nm core nanoparticles, whereas smaller symbols represent mixtures incorporating both 10 nm and 5 nm cores. (**b**) Calculated phase diagram of α versus γ at a fixed $\delta = 0.07$, which shows agreement with the experimental data. (**c**) Pair distribution function from simulations of PEG-functionalized flat walls with charged end groups illustrates electrostatic correlations. The prominent peak in the black curve reflects the hydrogen-bond-mediated attraction between COO^- and NH_3^+ groups (inset: typical hydrogen bonding geometry). The blue and green curves lack peaks, indicating strong repulsion between like-charged groups. (**d**) Simulation snapshot highlighting the attractive interaction between NH_3^+ and COO^- groups. (**e**) Simulation snapshot showing the repulsive interaction among NH_3^+ groups.

To this end, we performed all-atom molecular dynamics (MD) simulations, directly quantifying the electrostatic and hydrogen-bonding correlations that drive these forces. Our model system consists of planar walls (hypothetically NP surfaces) functionalized with PEG having COO^- or NH_3^+ end groups, neutralized by electrolytes. The justification for this model and further supporting results are provided in the SI. Fig. 4c shows the pair distribution function, $g(r)$, for COO^-–NH_3^+ pairs (solid black line), which exhibits a sharp peak indicating that roughly one-third of these end groups form bonds, with binding strength roughly independent of electrolyte concentration. This binding is enhanced by the formation of $COO^- \cdots NH_3^+$ hydrogen bonds. In contrast, Fig. 4d shows that equally charged end groups exhibit strong repulsion over distances up to nearly 1 nm, thereby validating the cutoff distance, r_c, used in our effective model (see Fig. 1a). Snapshot images in Fig. 4d further illustrate that similarly charged end groups remain well separated, effectively overcoming potential screening by electrolytes or charge neutralization by counterions. Together, these simulations illustrate the $B-B$ correlations, confirming the repulsive term assumed in Eq. 2, thus correcting the hard sphere model and leading to the phase diagram Fig. 4b.

Conclusions

By leveraging pH-regulated surface charge and controlling grafted-polymer conformation, we establish a generalizable, valence-free strategy for assembling open-framework cubic superlattices from binary mixtures of isotropic nanoparticles. In these systems, a single set of design rules, encoded in the nanoparticle size ratio γ and the grafted ligand molecular weight ratio θ, directs crystallization into lattices analogous to rock salt, CsCl, zinc blende, diamond, and even the rare simple cubic phase. SAXS measurements establish the exceptional structural quality, and our free-energy calculations and MD simulations quantitatively support the observed trends. Importantly, this approach is universally applicable to any nanoparticle–ligand system, enabling control over the lattice constant by tuning the core diameter and ligand molecular weight to adjust γ and θ. We demonstrated that our approach is scalable, as we have assembled a zinc-blende lattice with 5,10, and 20 nm nanoparticles, with a lattice constant ranging from 70 - 80 nm. Our versatile strategy introduces a new paradigm, realizing open architectures without directional bonding, and provides a general framework for designing functional nanoparticle superlattices for photonic to catalytic applications.

References

1. Macfarlane, R. J.; Lee, B.; Jones, M. R.; Harris, N.; Schatz, G. C.; Mirkin, C. A. Nanoparticle superlattice engineering with DNA. *science* **2011**, *334*, 204–208.

2. Macfarlane, R. J.; Jones, M. R.; Lee, B.; Auyeung, E.; Mirkin, C. A. Topotactic interconversion of nanoparticle superlattices. *Science* **2013**, *341*, 1222–1225.

3. Shevchenko, E. V.; Talapin, D. V.; Kotov, N. A.; O'Brien, S.; Murray, C. B. Structural diversity in binary nanoparticle superlattices. *Nature* **2006**, *439*, 55–59.

4. Kostiainen, M. A.; Hiekkataipale, P.; Laiho, A.; Lemieux, V.; Seitsonen, J.; Ruokolainen, J.; Ceci, P. Electrostatic assembly of binary nanoparticle superlattices using protein cages. *Nature nanotechnology* **2013**, *8*, 52–56.

5. Nykypanchuk, D.; Maye, M. M.; Van Der Lelie, D.; Gang, O. DNA-guided crystallization of colloidal nanoparticles. *Nature* **2008**, *451*, 549–552.

6. Bassani, C. L.; van Anders, G.; Banin, U.; Baranov, D.; Chen, Q.; Dijkstra, M.; Dimitriyev, M. S.; Efrati, E.; Faraudo, J.; Gang, O.; Gaston, N.; Golestanian, R.; Guerrero-Garcia, G. I.; Gruenwald, M.; Haji-Akbari, A.; Ibáñez, M.; Karg, M.; Kraus, T.; Lee, B.; Van Lehn, R. C. *et al.* Nanocrystal Assemblies: Current Advances and Open Problems. *ACS Nano* **2024**, *18*, 14791–14840.

7. Bian, T.; Gardin, A.; Gemen, J.; Houben, L.; Perego, C.; Lee, B.; Elad, N.; Chu, Z.; Pavan, G. M.; Klajn, R. Electrostatic co-assembly of nanoparticles with oppositely charged small molecules into static and dynamic superstructures. *Nature chemistry* **2021**, *13*, 940–949.

8. Boles, M. A.; Engel, M.; Talapin, D. V. Self-Assembly of Colloidal Nanocrystals: From Intricate Structures to Functional Materials. *Chemical Reviews* **2016**, *116*, 11220–11289.

9. Coropceanu, I.; Janke, E. M.; Portner, J.; Haubold, D.; Nguyen, T. D.; Das, A.; Tanner, C. P.; Utterback, J. K.; Teitelbaum, S. W.; Hudson, ̧ M. H.; others Self-assembly of nanocrystals into strongly electronically coupled all-inorganic supercrystals. *Science* **2022**, *375*, 1422–1426.

10. Liu, W.; Tagawa, M.; Xin, H. L.; Wang, T.; Emamy, H.; Li, H.; Yager, K. G.; Starr, F. W.; Tkachenko, A. V.; Gang, O. Diamond family of nanoparticle superlattices. *Science* **2016**, *351*, 582–586.

11. He, M.; Gales, J. P.; Ducrot, É.; Gong, Z.; Yi, G.-R.; Sacanna, S.; Pine, D. J. Colloidal diamond. *Nature* **2020**, *585*, 524–529.

12. Posnjak, G.; Yin, X.; Butler, P.; Bienek, O.; Dass, M.; Lee, S.; Sharp, I. D.; Liedl, T. Diamond-lattice photonic crystals assembled from DNA origami. *Science* **2024**, *384*, 781–785.

13. Kalsin, A. M.; Fialkowski, M.; Paszewski, M.; Smoukov, S. K.; Bishop, K. J. M.; Grzybowski, B. A. Electrostatic Self-Assembly of Binary Nanoparticle Crystals with a Diamond-Like Lattice. *Science* **2006**, *312*, 420–424.

14. Aguado, A.; Ayuela, A.; López, J. M.; Alonso, J. A. Structure and bonding in small neutral alkali halide clusters. *Physical Review B* **1997**, *56*, 15353.

15. Smart, L. E.; Moore, E. A. *Solid state chemistry: an introduction*; CRC press, 2012.

16. Hull, A. The Crystal Structure of Calcium. *Physical Review* **1921**, *17*, 42.

17. Desgreniers, S.; Beaulieu, L.; Lepage, I. Pressure-induced structural changes in ZnS. *Physical Review B* **2000**, *61*, 8726.

18. Leunissen, M. E.; Christova, C. G.; Hynninen, A.-P.; Royall, C. P.; Campbell, A. I.; Imhof, A.; Dijkstra, M.; van Roij, R.; van Blaaderen, A. Ionic colloidal crystals of oppositely charged particles. *Nature* **2005**, *437*, 235–40.

19. Rechtsman, M. C.; Stillinger, F. H.; Torquato, S. Synthetic diamond and wurtzite structures self-assemble with isotropic pair interactions. *Physical Review E* **2007**, *75*, 031403.

20. Rechtsman, M. C.; Stillinger, F. H.; Torquato, S. Self-assembly of the simple cubic lattice with an isotropic potential. *Physical Review E - Statistical, Nonlinear, and Soft Matter Physics* **2006**, *74*, 021404.

21. Lin, Y.; Olvera de la Cruz, M. Superionic colloidal crystals: Ionic to metallic bonding transitions. *The Journal of Physical Chemistry B* **2022**, *126*, 6740–6749.

22. Nayak, B. P.; Zhang, H.; Bu, W.; Ocko, B. M.; Travesset, A.; Vaknin, D.; Mallapragada, S. K.; Wang, W. Ionic-like Superlattices by Charged Nanoparticles: A Step Toward Photonics Applications. *ACS Applied Nano Materials* **2024**, *7*, 3220–3228.

23. Travesset, A. Nonlinear Poisson–Boltzmann solutions for charged parallel plates: When opposite charges repel. *The Journal of Chemical Physics* **2024**, *161*, 054903.

24. Ho, K.; Chan, C. T.; Soukoulis, C. M. Existence of a photonic gap in periodic dielectric structures. *Physical Review Letters* **1990**, *65*, 3152.

25. Zha, X.; Travesset, A. The Hard Sphere Diameter of Nanocrystals (Nanoparticles). *Journal of Chemical Physics* **2020**, *152*, 094502.

26. Kim, H. J.; Wang, W.; Zhang, H.; Freychet, G.; Ocko, B. M.; Travesset, A.; Mallapragada, S. K.; Vaknin, D. Effect of polymer chain length on the superlattice assembly of functionalized gold nanoparticles. *Langmuir* **2021**, *37*, 10143–10149.

27. Nayak, B. P.; Batey, J. E.; Kim, H. J.; Wang, W.; Bu, W.; Zhang, H.; Mallapragada, S. K.; Vaknin, D. Effect of grafting density on the two-dimensional assembly of nanoparticles. *Applied Surface Science* **2025**, 162556.

28. Lai, K. C.; Zha, X.; Evans, J. W.; Travesset, A. Structure of Polydisperse fcc Nanocrystals: Implications for Crystal Fractionalization. *The Journal of Physical Chemistry C* **2019**, *123*, 9528–9537.

29. Cabane, B.; Li, J.; Artzner, F.; Botet, R.; Labbez, C.; Bareigts, G.; Sztucki, M.; Goehring, L. Hiding in plain view: colloidal self-assembly from polydisperse populations. *Physical review letters* **2016**, *116*, 208001.

30. Nayak, B. P.; Kim, H. J.; Travesset, A.; Vaknin, D.; Mallapragada, S. K.; Wang, W. Tuning Self-Assembly of Gold Nanoparticles Grafted with Charged Polymers by Varying Temperature and Electrolytes. *The Journal of Physical Chemistry C* **2023**, *127*, 24651–24657.

31. Zhang, H.; Wang, W.; Mallapragada, S.; Travesset, A.; Vaknin, D. Macroscopic and Tunable Nanoparticle Superlattices. *Nanoscale* **2017**, *9*, 164–171.

32. Nayak, B. P.; Kim, H. J.; Nayak, S.; Wang, W.; Bu, W.; Mallapragada, S. K.; Vaknin, D. Assembling PNIPAM-Capped Gold Nanoparticles in Aqueous Solutions. *ACS Macro Letters* **2023**, *12*, 1659–1664.

33. Kim, H. J.; Wang, W.; Travesset, A.; Mallapragada, S. K.; Vaknin, D. Temperature-induced tunable assembly of columnar phases of nanorods. *ACS nano* **2020**, *14*, 6007–6012.

34. Morozova, S. M.; López-Flores, L.; Gevorkian, A.; Zhang, H.; Adibnia, V.; Shi, W.; Nykypanchuk, D.; Statsenko, T. G.; Walker, G. C.; Gang, O.; others Colloidal Clusters and Networks Formed by Oppositely Charged Nanoparticles with Varying Stiffnesses. *ACS nano* **2023**, *17*, 15012–15024.

35. Anderson, J. A.; Lorenz, C. D.; Travesset, A. General purpose molecular dynamics simulations fully implemented on graphics processing units. *Journal of Computational Physics* **2008**, *227*, 5342–5359.

36. Travesset, A. Phase diagram of power law and Lennard-Jones systems: Crystal phases. *The Journal of Chemical Physics* **2014**, *141*, 164501.

37. Upah, A.; Thomas, A.; Hallstrom, J.; Travesset, A. High-Precision Calculation of Nanoparticle (Nanocrystal) Potentials of Mean Force and Internal Energies. *Journal of Chemical Theory and Computation* **2024**, *20*, 1559–1567.

38. Nguyen, T. D.; Phillips, C. L.; Anderson, J. A.; Glotzer, S. C. Rigid body constraints realized in massively-parallel molecular dynamics on graphics processing units. *Computer Physics Communications* **2011**, *182*, 2307–2313.

39. Jorgensen, W. L.; Maxwell, D. S.; Tirado-Rives, J. Development and testing of the OPLS all-atom force field on conformational energetics and properties of organic liquids. *Journal of the American Chemical Society* **1996**, *118*, 11225–11236.

40. Klein, C.; Summers, A. Z.; Thompson, M. W.; Gilmer, J. B.; McCabe, C.; Cummings, P. T.; Sallai, J.; Iacovella, C. R. Formalizing atom-typing and the dissemination of force fields with foyer. *Computational Materials Science* **2019**, *167*, 215–227.

41. Boerner, T. J.; Deems, S.; Furlani, T. R.; Knuth, S. L.; Towns, J. ACCESS: Advancing Innovation. *Practice and Experience in Advanced Research Computing* **2023**, 173–176.

42. Kjellander, R. A multiple decay-length extension of the Debye-Hückel theory: To achieve high accuracy also for concentrated solutions and explain under-screening in dilute symmetric electrolytes. *Physical Chemistry Chemical Physics* **2020**, *22*, 23952–23985.

Materials and Methods

Materials

Unconjugated citrate-capped AuNPs of nominal core diameters of 5 and 10 nm were purchased from Ted Pella Inc., and their size distributions were verified independently by TEM (5.8 ± 0.6 and 9.1 ± 1, respectively, See Figs. S4-S5) and by SAXS.[30] PEG with an average molecular weight of 2, 5, and 10 kDa, modified with a thiol (HS) group at one end and either a carboxyl ($-$COOH) or amine ($-NH_2$) group at the other, was purchased from Creative PEGworks (NC, USA) and used without further purification. HCl was purchased from Fisher Scientific and used without further purification. Milli-Q water (resistivity 18.2 MΩ·cm at 25 °C) was used in all experiments.

PEG Grafting to AuNPs Surfaces

AuNPs are functionalized with HS-PEG-COOH or HS-PEG-NH_2 using a ligand exchange protocol, as described previously.[27,31] Briefly, PEG ligands were dissolved in water and thoroughly mixed to form a homogeneous suspension. This PEG solution, in molar excess, was added to AuNP suspensions at a 1:1500 AuNP-to-PEG chain ratio for 5 nm AuNPs and a 1:6000 ratio for 10 nm AuNPs. The mixture was rotated overnight at ∼35 RPM on a Roto-Shake Genie (Scientific Industries, NY, USA) under continuous mixing to facilitate ligand exchange. Unbound PEG was removed from the PEG-functionalized AuNPs by three rounds of centrifugation. For 5 nm AuNPs, centrifugation was performed at 21,000 ×g for 90 minutes per round, while for 10 nm AuNPs, it was conducted at 20,000 ×g for 75 minutes. After centrifugation, the resulting PEG-grafted AuNPs were resuspended in Milli-Q water to create a stock suspension. The final concentration of the PEG-AuNP suspensions was determined by measuring absorbance using ultraviolet-visible (UV-vis) spectroscopy (NanoDrop One Microvolume, Thermo Fisher Scientific). Concentrations were adjusted to approximately 20 nM for 10 nm AuNPs and 80 nM for 5 nm AuNPs, as described below.

The molarity of AuNP suspensions is calculated using the concentration data provided by the supplier (TedPella Inc.), which specifies the number of particles per milliliter of solution. The following equation is employed for the calculation:

$$\text{Molarity (M)} = \frac{\text{Number of particles per ml}}{N_{\text{A}} \times 10^{-3} \text{ liters}} \tag{3}$$

where N_{A} is Avogadro's number.
For instance, the molarity of 10 nm-sized bare AuNPs is determined from the particle concentration provided in the vendor's technical data sheet, which is 5.7×10^{12} particles/ml. Using Eq. 3, the molarity is calculated to be 9.46 nM. After determining the molarity of the bare AuNPs, UV-vis spectrophotometry is utilized to determine their absorbance at a wavelength of 525 nm. Assuming that the grafting of PEG does not influence the absorbance and that no aggregation occurs, the absorbance profiles of the PEG-grafted AuNPs can be compared with those of the bare AuNPs to determine the concentration of the grafted AuNPs in suspension.

In this study, "PEG-AuNP" refers to PEG-grafted AuNPs in general, while x-PEGy-AuNPz specifies the detailed characteristics of the nanoparticles. In this labeling scheme, z represents the core diameter of the AuNPs in nanometers (e.g., 5 or 10 nm), y refers to the molecular weight of the grafted PEG (2, 5 or 10 kDa), and x indicates the terminal functional group of the PEG chain ($-$COOH or $-NH_2$). For example, COOH-PEG5k-Au10 describes 10 nm AuNPs functionalized with 5 kDa PEG terminated with a carboxyl group ($-$COOH). Similarly, NH_2-PEG10k-Au5 denotes 5 nm AuNPs grafted with 10 kDa PEG terminated with an amine group ($-NH_2$). The complete labeling scheme and detailed properties of all PEG-grafted nanoparticles are provided in Table S1. The legend for each PEG-AuNPs is depicted as a hard sphere in Fig. 1b.

DLS and $\zeta-$potential Measurements

The hydrodynamic diameter (D_{H}) of grafted nanoparticles was measured by dynamic light

scattering (DLS) on a NanoZS90 with Zetasizer software (Malvern, UK). Zeta potential measurements, conducted on the same instrument, were used to quantify the surface charge of PEG-grafted AuNPs. These data are summarized in Table S1. Successful PEG grafting with distinct terminal groups ($-$COOH or $-NH_2$) was confirmed by observing opposite surface charges and increased hydrodynamic sizes. Further details on PEG grafting and characterization are available in a recent publication.[22] While hydrodynamic diameters and the DLS-derived size ratio γ provide objective, experimentally measurable design parameters to guide nanoparticle assembly, they are not expected to exactly predict the resulting lattice constants, which are ultimately governed by collective packing effects, polymer deformation, and electrostatic interactions.

Surface Charge Manipulation

To adjust the surface and overall charge of the grafted AuNPs, HCl was added to the suspensions, achieving final concentrations of 0.1, 1, and 10 mM. Since the small sample volumes required for SAXS hinder direct pH measurement, HCl concentrations and corresponding estimated pH values are specified in parentheses. For SAXS, a calculated volume of AuNP suspension was mixed in a glass scintillation vial at the desired mixing ratio. Mixing ratio are calculated in terms of NP number ratios. Stock HCl solutions were added to the AuNP mixture, thoroughly mixed, and incubated for $\sim$ 20 minutes. The mixture was then loaded into a quartz capillary ($\sim$ 1.5 mm diameter) for SAXS measurements.

SAXS Measurements

Fig. 5 illustrates the procedure for creating binary mixtures, conducting the small-angle X-ray scattering (SAXS) measurements, and their structural analysis. *In situ* SAXS was employed to determine the structures formed in the suspensions at various pH levels and temperatures. Given the lower electron density (ED) of the polymers compared to gold, the diffraction is dominated by the AuNPs. We employed AuNPs of two distinct sizes (10 nm and 5 nm) to achieve scattering contrast in our binary mixtures. In contrast, when the binary system comprises of nanoparticles with identical core sizes (10 or 5 nm), the resulting superstructures exhibit a uniform, single-particle-like lattice (such as a diamond or simple cubic lattice). For a general binary system, we designate the constituent particles as $\mathcal{A}$ and $\mathcal{B}$, where $D_A > D_B$, without specifying their precise sizes or the details of their PEG ligand terminations.

Synchrotron-based *in situ* SAXS experiments were conducted at beamline 12-ID-B of the Advanced Photon Source (APS), Argonne National Laboratory, and at the 11-BM CMS end station of the National Synchrotron Light Source II (NSLS-II), Brookhaven National Laboratory. The incident X-ray energies were 13.3 keV and 13.5 keV, respectively. Bench-top *in situ* SAXS was performed using a liquid-metal-jet Ga alloy source with an incident X-ray energy of 9.2 keV.

Incubated samples were transferred into $\sim$1.5 mm diameter quartz capillaries and positioned vertically in beamline-specific sample holders, normal to the incident beam. Data acquisition and processing were carried out following each beamline's protocol. SAXS data were reduced to one-dimensional (1D) scattering profiles as a function of the wave vector magnitude Q, where $Q = 4\pi \sin\theta/\lambda$, with 2θ being the scattering angle and λ the X-ray wavelength. Details of the experimental setup, data acquisition, and analysis protocols are available in previous studies.[32–34]

The scattering profiles, $I(Q)$, were background-corrected by subtracting signals from corresponding water samples, resulting in diffraction patterns resembling those of polycrystalline samples in suspension. The plotted scattering profiles are presented as raw $I(Q)$ after only background subtraction; no form-factor correction $P(Q)$ was applied owing to the dominance of long-range order scattering, and structural assignments are based on peak positions, with relative intensities noted but not used as the sole determinant. Data analysis followed standard procedures for X-ray diffraction of poly-

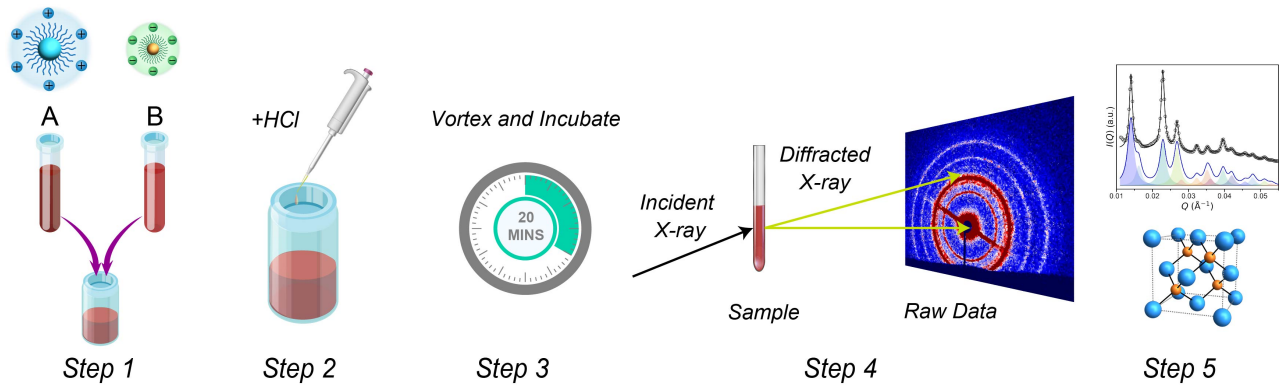

Fig. 5. Schematic illustration of the standard procedure for creating and characterizing superstructures by SAXS. (1) Prepare the binary system using specified mixing ratios. (2) Adjust the pH of the mixture. (3) Thoroughly mix and incubate the suspension. (4) Load the mixture into a capillary and expose it to a monochromatic X-ray beam, resulting in a ring-like diffraction pattern characteristic of polycrystalline samples. (5) Convert the ring pattern to 1D $I(Q)$ versus Q scattering plots and assign the corresponding superlattice structure.

crystalline materials. For crystalline samples, peak positions were identified based on expected reflections for specific space groups, and structure factors were calculated and fitted to the data to determine the fundamental unit cell dimensions and particle occupancy. Based on structural organization, we classified the assemblies as long-range ordered (LRO) for crystalline domains larger than 10 unit cells, meso-range ordered (MRO) for 5-10 unit cells, and short-range ordered (SRO) for domains smaller than 5 unit cells.[22]

All-atom Molecular Dynamics Simulations

All-atom molecular dynamics simulations using HOOMD-blue[35] implemented through HOODLT.[36,37] HOODLT was used to generate the initial configurations, implement the force field, and analyze the results. The system consisted of two parallel plates composed of gold atoms, modeled as rigid bodies[38] and grafted with PEG ligands terminating in charged end groups with the addition of salt (NaCl) in different concentrations, see justification of the model further below. The OPLS force field[39] implemented through Foyer[40] was used. We simulated three distinct systems: (a) a system with 98 PEG ligands in total 49 on each plate where one plate terminated in COO^- and the other in NH_3^+ groups; (b) a system with 98 PEG ligands all terminating in COO^- groups with Na^+ as counterions; and (c) a system with 98 PEG ligands all terminating in NH_3^+ groups with Cl^- as counterions. Each system was simulated at varying plate separations ranging from 4.6 nm to 11.6 nm, and at salt molalities of 0.5 and 1.1 mol/kg, with SPC/E water used as the solvent. All simulations were first equilibrated in the NPT ensemble for 3 ns using the MTTK thermostat and barostat to maintain constant temperature and pressure. This was followed by 40 nanoseconds of production run in the NVT ensemble with the same MTTK thermostat with a timestep of 1 fs. All simulations were conducted on the Bridges-2 high-performance computing cluster at the Pittsburgh Supercomputing Center.

Supporting Information

The supporting information PDF file includes the following information:

- Supplementary Text
- Figures S1-S34
- References 30-42

Data Availability

The findings of this study are supported by the data found in the article and the Supplementary Information provided. Further relevant in-

formation and source data can be obtained from the link below.

Acknowledgements

This work was supported by the U.S. Department of Energy (DOE), Office of Science, Basic Energy Sciences, Materials Science and Engineering Division. The research was performed at the Ames National Laboratory, which is operated for the U.S. DOE by Iowa State University under contract No. DE-AC02-07CH11358. The authors thank the beamline staff team at 12-ID-B for the synchrotron beamline support at the Advanced Photon Source (APS), Argonne National Laboratory. Part of this research used beamline 12-ID-B of the APS, a U.S. DOE Office of Science user facility at Argonne National Laboratory and is based on research supported by the U.S. DOE Office of Science-Basic Energy Sciences, under Contract No. DE-AC02-06CH11357. Part of this research used the Complex Materials Scattering (CMS) Beamline (CMS, Beamline 11-BM) of the National Synchrotron Light Source II, and the Materials Synthesis and Characterization Facility of the Center for Functional Nanomaterials (CFN), which is a U.S. DOE Office of Science User Facility, at Brookhaven National Laboratory under Contract No. DE-SC0012704.

Part of this work used the BRIDGES2 GPU cluster through allocation MCB140071 from the Advanced Cyberinfrastructure Coordination Ecosystem: Services Support (ACCESS) program,[41] which the National Science Foundation supports grants 2138259, 2138286, 2138307, 2137603, and 2138296. Work by ZM and SZ was supported by the U.S. DOE, Office of Science, Office of Basic Energy Sciences, Established Program to Stimulate Competitive Research (EPSCoR) Program under Award Number DE-SC0025585.

Author contributions

WW, DV, AT, and SM conceived and supervised the project. BN, DV, and WW designed, conducted the experiments, and analyzed the data. BN, WW, AT, and DV wrote the manuscript. AT developed the theoretical/computational models, and PK performed all the atom simulations. HZ and DN helped conduct the SAXS experiments. ZM and SZ performed complementary electron microscopy imaging experiments. SM, DV, AT, and WW secured the funding for the project. All co-authors read and reviewed the manuscript.

Competing interests

The authors declare that they have no competing interests.

Supplementary Files

This is a list of supplementary files associated with this preprint. Click to download.

- SI.pdf